Optics Letters

Symmetric metasurface with dual band polarization-independent high-Q resonances governed by symmetry-protected BIC

YUEPEI CAI, YONG HUANG,* KEYONG ZHU, AND HUIHAI WU

Aeronautic Science and Engineering, Beihang University, Beijing 100191, China
**Corresponding author: huangy@buaa.edu.cn*

Received 20 May 2021; revised 11 July 2021; accepted 12 July 2021; posted 12 July 2021 (Doc. ID 432117); published 13 August 2021

In this Letter, we propose a symmetric metasurface composed of single-sized amorphous-silicon (a-Si) cuboids tetramer clusters that support two resonances with opposite symmetry, i.e., in-plane magnetic dipole (MD) resonance and in-plane toroidal dipole (TD) resonance governed by symmetry-protected bound states in the continuum (SP-BIC) in the near-infrared region. Since the cuboids tetramer of the metasurface retains C_{4v} symmetry and mirror symmetry, both resonances are polarization independent. Multipolar decomposition of scattering power and electromagnetic distribution are performed to clarify the physical mechanism of dual quasi-BIC resonances. The effects of geometric parameters on both high-quality (Q) resonances are also studied. Additionally, the sensing performance of the designed metasurface is evaluated. The effects of the material's loss on both resonances are also studied. Our work provides a new route to designing dual mode polarization-independent resonators without multi-sized complex structures that may facilitate designing high-performance sensing applications.

https://doi.org/10.1364/OL.432117

High-Q resonance in nanophotonics has attracted growing attention over the past decade because of its promising use in applications ranging from narrow-band filtering [1], slow-light devices [2], nonlinear optics interaction enhancement [3] to highly sensitive sensing [4]. High-Q resonance structures such as photonic crystals [5], guided-mode gratings [6], Fabry–Perot resonators [7], ring resonators [8], and whispering-gallery resonators [9] are usually based on the total internal reflection principle and work below the light line. Previous approaches to high-Q resonance design imposed intrinsic drawbacks of high-volume cavities or large-scale bending radii [10]. Recently, a new route to designing high-Q resonances based on asymmetric metasurfaces [11] that are related to the BIC phenomenon has garnered much attention because its exotic optical properties allow it to work above the light line.

Bound states in the continuum (BIC) was originally proposed in quantum mechanics to describe the isolated eigenvalues of single-particle Schrödinger equations embedded in the continuum of positive energy states [12]. Then it was extended to classical wave physics including acoustics, electromagnetics, hydrodynamics, elastic waves, and optics [13]. BIC can be regarded as a resonant state with zero linewidth and infinite radiative Q factors. In optics, BIC is a phenomenon where light can be perfectly localized even above the light line. Ideal BIC cannot be observed from the electromagnetic spectrum because of its nonradiative intrinsic features with vanishing resonance linewidths.

By breaking the symmetry of structures, SP-BIC can be perturbed and then transformed into quasi-BIC, which can radiate to the external continuum and produce high-Q resonances when near-field distribution slightly deviates from symmetric modes [14]. Resonances governed by the SP-BIC are frequently polarization sensitive [15–17] because the in-plane symmetry perturbation [18,19] and out-of-plane symmetry perturbation [20,21] required for their excitation always breaks the rotational symmetry, or mirror symmetry, of the structures. To design polarization- insensitive resonances driven by SP-BIC, metasurfaces consisting of a nanodisk multimer supercell [22–24], a radius asymmetric perforated holes array in a high-refractive-index slab [25], and a reduced symmetry hexagonal high-index-contrast grating [26] were employed. However, the aforementioned symmetry perturbated structures are not easy to design and fabricate when compared to single-sized regular geometry. Recently, polarization-independent SP-BIC was excited in metasurfaces made of equidistantly spaced perturbed high-refractive-index dielectric disks array [27]. This symmetric perturbation method without losing C_{4v} features was encouraging. However, only single-mode resonance may limit its application.

In this Letter, we demonstrate that polarization-independent dual-mode resonances that are governed by SP-BIC can be induced in single-sized cuboids tetramer metasurface with C_{4v} features. More importantly, metasurfaces with dual BICs, which can modify line shapes at two resonance wavelengths simultaneously, are quite suitable for nonlinear optics and multiwavelength sensing [28]. We also noted that dual resonances of the metasurface are with opposite symmetry, and such a system with opposite symmetry may support degenerate critical coupling phenomena [29].

As shown in Fig. 1(a), four square unit cells with the same geometric parameters are arranged into a 2 × 2 square supercell. Geometric parameters include the period of the single-unit cell

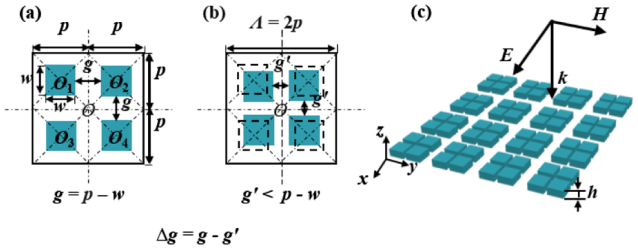

Fig. 1. Schematic of the supercell consisting of four same square unit cells when (a) $g = p - w$ and (b) g is changed to g'. (c) Schematic of the metasurface with thickness h- and x-polarized normal incidence light.

p, the width of the a-Si cuboid w, and the gap distance between neighboring cuboids in supercell g. The center of each cuboid and the center of each unit cell is coincident in O_1, O_2, O_3, and O_4, respectively, i.e., $g = p - w$. In this state, the minimal period of the whole structure is p, and each unit cell retains its C_{4v} symmetry and mirror symmetry. To cause a symmetry perturbation of the whole structure without losing the C_{4v} symmetry and mirror symmetry, four cuboids are moved toward the center of the supercell O simultaneously, as shown in Fig. 1(b), i.e., p and w remain unchanged, whereas g varies to g'. After the operation provided in Fig. 1(b), the minimal period of the whole structure changes from p to $\Lambda = 2p$.

As a demonstration, we set the metasurface depicted in Fig. 1(c) with geometry parameters $p = 500$ nm, $w = 300$ nm, $g = 200$ nm, and $h = 200$ nm. The refractive index of the a-Si is set as 3.42 [30]. The asymmetry parameter is $\alpha = \Delta g/g$, where $\Delta g = g - g'$ represents the gap-distance difference between the original state and the present state. A numerical calculation was performed utilizing COMSOL with periodic conditions applied in both x and y directions of the unit cell, and the perfectly matched layer condition was applied above and under the unit cell. The calculated transmission spectra of varying Δg ranging from 0 to 160 nm with a 40 nm step are plotted in Fig. 2(a). Clearly, for $\Delta g = 0$ nm (i.e., $g = 200$ nm and $\alpha = 0$), no transmission dips can be observed, and the linewidth vanishes. As the Δg increases, the transmission spectra show two distinct Fano line-shape resonances, and its linewidth increases. Meanwhile, the two resonant wavelengths both shift toward longer wavelengths as the Δg increases.

In Figs. 2(b) and 2(c), the relationship between the Q factor and the asymmetry parameter, α, of both modes is investigated. The dependence of the Q factor on α of both modes met the inverse quadratic law, i.e., $Q \propto \alpha^{-2}$, which is consistent with previous research [31]. This also demonstrates that both

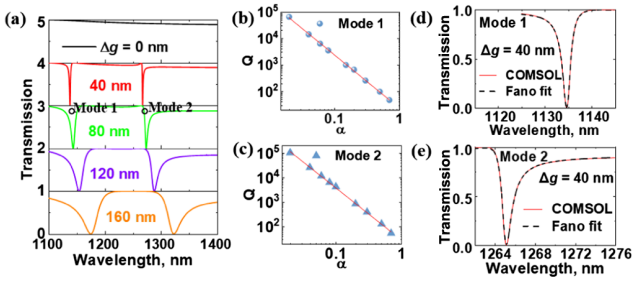

Fig. 2. (a) Evolution of the transmission spectra versus Δg. Log-log plot of Q as a function of the α of (b) Mode 1 and (c) Mode 2. Fano fitting of (d) Mode 1 and (e) Mode 2.

Mode 1 and Mode 2 are governed by SP-BIC. Two asymmetric resonances originated from the interference between discrete states of tetramer metasurfaces and the continuum-free space. In Figs. 2(d) and 2(e), we fit the curves of Mode 1 and Mode 2 when $\Delta g = 40$ nm with the classical Fano formula

$$T(\omega) = T_0 + A_0 \frac{[q + 2(\omega - \omega_0)/\tau]^2}{1 + [2(\omega - \omega_0)/\tau]^2}, \tag{1}$$

where T_0 is the transmission offset, A_0 is the continuum-discrete coupling constant, q represents the Breit–Wigner–Fano parameters, ω_0 is the resonant wavelength, and τ is the resonant linewidth. The Q of Mode 1 and Mode 2 at $\Delta g = 40$ nm can be evaluated with $Q = \omega_0/\tau$ and derived from $Q_{MD} = 551$ and $Q_{TD} = 1137$.

To gain additional insight into the mechanism of the two quasi-BIC mode resonances, the scattering powers of different multipoles including the electric dipole (ED), the magnetic dipole (MD), the toroidal dipole (TD), the electric quadrupole (EQ), and the magnetic quadrupole (MQ) in the Cartesian coordinate system were calculated [32] and plotted in Figs. 3(a)–3(d). For Mode 1, it can be observed clearly that the contribution of the MD (red solid line) is dominant, which indicates that Mode 1 is mainly induced by the MD, as shown in Fig. 3(a). By decomposing the x, y, and z components of the MD scattering powers in Fig. 3(b), we find that the y component of scatter power from the MD is predominant in the MD scatter power and nearly equals to it in value. Whereas the x and z components of scatter power from the MD approaches zero when compared to the y component. This indicates that the MD moment is along the y direction when the metasurface is illuminated by x-polarized light. For Mode 2, the TD is

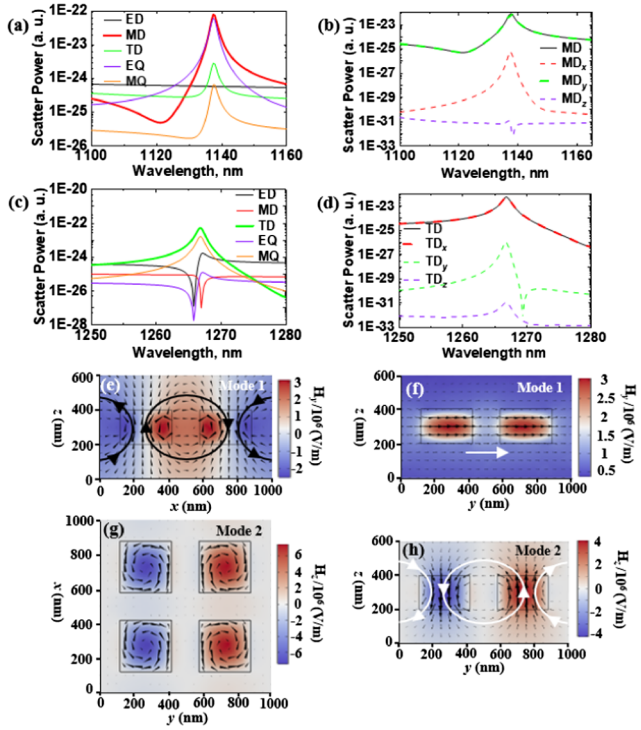

Fig. 3. Scattered powers near Mode 1 from (a) multipoles and (b) x, y, and z components of the MD. Scattered powers near Mode 2 from (c) multipoles (d) x, y, and z components of the TD. Electromagnetic field distribution of Mode 1 (e),(f) and Mode 2 (g),(h).

predominant and the TD moment is along the x direction, as depicted in Figs. 3(c) and 3(d).

Electromagnetic field distributions of the metasurface at the corresponding resonance mode are visualized in Figs. 3(e)–3(h). The black cones represent the displacement current density, and the white arrows represent the magnetic field vector. For Mode 1, displacement currents are circulated in a clockwise circulation manner between the intra-cluster x direction neighboring cuboids and counterclockwise in the inter-cluster x direction neighboring cuboids, as shown in Fig. 3(e). Displacement currents distribute in a head-to-tail manner, which is a characterization of the MD resonance, and the direction of the MD is along the y direction according to the right-hand screw rule, which is consistent with the far-field analysis and the magnetic vectors in the $y-z$ plane plotted in Fig. 3(f). For Mode 2, as shown in Fig. 3(g), circulation orientations of displacement currents in the y direction of the Si neighboring cuboids are opposite and the same in the x direction of the neighboring cuboids, which indicates that the opposite phase magnetic dipoles along the z direction are induced in the y direction cuboids pair. Figure 3(h) depicts the magnetic field distribution at the $y-z$ plane. Opposite-phase magnetic dipoles form a closed magnetic vortex in the $y-z$ plane. Magnetic field vectors are circulated in a counterclockwise circulation manner between the intra-cluster y direction neighboring cuboids and clockwise in the inter-cluster y direction neighboring cuboids. Magnetic field vector distributes in a head-to-tail manner, which is a characterization of the TD resonance, and the direction of the TD is along the x direction according to the right-hand screw rule. As we have mentioned before, such dual resonances are with opposite symmetry (y direction in-plane MD and x direction in-plane MD).

In fact, when g is set to a constant, the variation of Λ or w can also cause symmetry perturbation. It should be noted that Λ is related to the electromagnetic diffraction directly [33], and w has a strong effect at the scattering property of each cuboid resonator [34]. Thus the influence of p and w on the two modes is very complex. Q no longer obeys the inverse-square dependence rules on the asymmetric parameters when varying p or w. It can be seen from Fig. 4(a) that both Mode 1 and Mode 2 resonance wavelengths red shift when Λ is increased from 1050 to 1250 nm. The linewidth of Mode 2 increases noticeably when compared to Mode 1. On the contrary, when w decreases from 280 to 200 nm, both mode resonance wavelengths blue shift. The linewidth of Mode 1 increases noticeably when compared to Mode 2.

The thickness of the metasurface h does not affect the symmetry of the structure, and it can be used to tune the resonance wavelength of both modes. As a demonstration, we chose base case geometric parameters as $g' = 160$ nm, $p = 1000$ nm, $w = 300$ nm, and $h = 200$ nm. As shown in Fig. 4(c), increasing h from 180 to 220 nm resulted in the red shift of both resonances in a linear manner, while their linewidths changed little. Another way to tune the resonance wavelength without changing the asymmetry parameter is to increase, or decrease, the geometrical parameters by simultaneously multiplying them (p, w, g, and h) with a scaling factor F (farad). It can be seen in Fig. 4(d) that both resonances shift to the longer wavelengths linearly when the scaling factor increases, while their linewidth remain nearly unchanged.

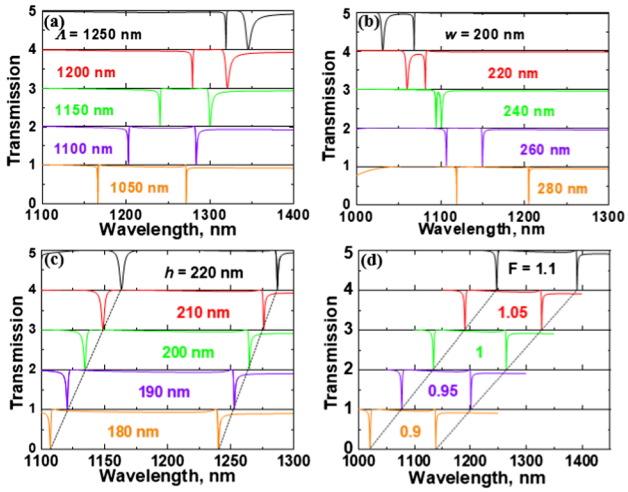

Fig. 4. Evolution of the transmission spectra versus (a) Λ, (b) w, (c) h, and (d) F.

Both resonant wavelengths of the metasurface are dependent on the surrounding background medium, which is promising for gas-sensing applications [35]. Based on this, we designed a metasurface gas sensor composed of Si cuboids tetramer clusters, a low refractive index dielectric substrate (MgF_2 with the refractive index unit (RIU) set as 1.38), and an integrated microfluidic channel, as shown in Fig. 5(a) [36,37]. This metasurface can be fabricated by depositing a-silicon film onto the MgF_2 substrate by means of low-pressure chemical-vapor deposition and subsequent patterning of the silicon layer via standard electron-beam lithography (EBL) or reactive ion etching (RIE) [38]. In the calculation, supposing that the EBL system with the mediocre performance is chosen and the geometric parameters of the metasurface gas sensor are set as $\Lambda = 1000$ nm, $w = 300$ nm, $h = 200$ nm, and $g' = 190$ nm (i.e., $\Delta g = 10$ nm and $\alpha = 0.05$), the sensing performance can be evaluated with sensitivity, $S = \Delta\lambda/\Delta n$, and figure of merit, FOM = S/FWHM, where $\Delta\lambda$ is the resonance peak wavelength shift, and Δn is the refractive index change of the analyte gas.

As shown in Fig. 5(b), increasing the refractive index of gas from 1.01 to 1.09 can cause a red shift of the resonant wavelength, λ_{MD}, from 1250.00 to 1292.10 nm, with the FWHM being smaller than 0.07 nm and the step interval, $\Delta\lambda$, being about 10.28 nm. The resonant wavelength, λ_{TD}, red shifts from 1317.48 to 1342.41 nm, with the FWHM being smaller than 0.09 nm and the step interval, $\Delta\lambda$, being about 6.23 nm. The analyte index ranging from 1.3 to 1.4, which covers most aqueous and alcohol solutions relevant for refractometry, is considered in Fig. 5(c). Both resonant wavelengths show linear dependence rule with a calculated $S_{MD} = 613$ nm/RIU and a $S_{TD} = 535$ nm/RIU in this considered wavelength range, and the FOM of the MD mode and the TD mode can achieve 34056 and 4534, respectively. When considering a broader range of analyte index ranging from 1 to 1.4, the sensor's linearity deteriorates, as shown in Fig. 5(d). But with a narrower range, such as 1–1.1, linear dependence still works well with the slope of the linear fitting in this range, $S_{MD} = 526$ nm/RIU and $S_{TD} = 312$ nm/RIU. The FOM of the MD mode and the TD mode can achieve 8092 and 3387, respectively, in this range. We also considered the loss effect of a-Si cuboids on both

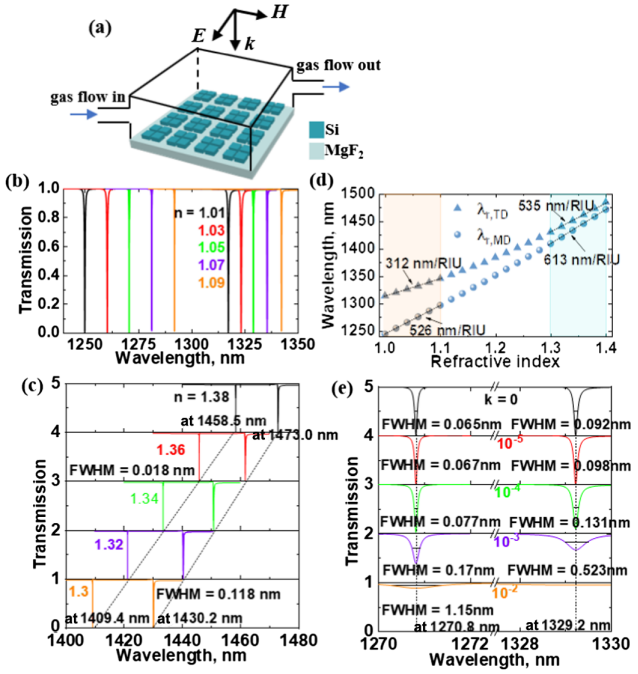

Fig. 5. (a) Schematic of the metasurface with a MgF_2 substrate. Transmission spectra versus the refractive index of gas (b) 1–1.1 and (c) 1.3–1.4. (d) Transmission peak wavelengths as a function of the gas's refractive index. (e) Evolution of the transmission spectra versus loss k.

resonances. As shown in Fig. 5(e), with the refractive index of sensing air set as 1.05, when the loss of cuboids k increases, especially when $k > 10^{-3}$, the FWHM increases noticeably, and both resonances wavelength remain nearly unchanged. Q can be evaluated by $Q = \omega_0/\mathrm{FWHM}$. Thus larger k progressively deteriorates the Q and the FOM. Transmission is also reduced, especially at the resonance wavelength when increasing k. In reality, metasurfaces that consist of square unit cells are generally fabricated in finite size and consists of $N \times N$ unit cells. Q can be boosted up by increasing N. Thus, to derive a high-Q resonance, the metasurface should be fabricated with $N > 15$, as illustrated by Liu *et al.*'s results [31].

In summary, symmetric metasurfaces composed of single-sized cuboids tetramer clusters were proposed, and the mechanisms of both the quasi-BIC modes were analyzed by multipolar decomposition of scattering powers and near-field distributions. The effects of the geometric parameters on the resonances were also studied. The performance of the designed metasurface sensor shows that its gas-sensing ability is very promising.

Funding. National Natural Science Foundation of China (51876004).

Disclosures. The authors declare no conflicts of interest.

Data Availability. Data underlying the results presented in this paper are not publicly available at this time but may be obtained from the authors upon reasonable request.

REFERENCES

1. K. Kawanishi, A. Shimatani, K. J. Lee, J. Inoue, S. Ura, and R. Magnusson, Opt. Lett. **45**, 312 (2020).
2. J. Gu, R. Singh, X. Liu, X. Zhang, Y. Ma, S. Zhang, S. A. Maier, Z. Tian, A. K. Azad, H.-T. Chen, A. J. Taylor, J. Han, and W. Zhang, Nat. Commun. **3**, 1151 (2012).
3. Y. Chen, L. Dong, X. Xu, J. Jiang, and Y. Shi, J. Appl. Phys. **122**, 244507 (2017).
4. P. K. Sahoo, S. Sarkar, and J. Joseph, Sci. Rep. **7**, 7607 (2017).
5. B.-S. Song, T. Asano, S. Jeon, H. Kim, C. Chen, D. D. Kang, and S. Noda, Optica **6**, 991 (2019).
6. A. Ferraro, D. C. Zografopoulos, R. Caputo, and R. Beccherelli, Sci. Rep. **8**, 17272 (2018).
7. X. Chen, C. Chardin, K. Makles, C. Caër, S. Chua, R. Braive, I. Robert-Philip, T. Briant, P.-F. Cohadon, A. Heidmann, T. Jacqmin, and S. Deléglise, Light Sci. Appl. **6**, e16190 (2017).
8. X. Ji, F. A. S. Barbosa, S. P. Roberts, A. Dutt, J. Cardenas, Y. Okawachi, A. Bryant, A. L. Gaeta, and M. Lipson, Optica **4**, 619 (2017).
9. X. Jiang and L. Yang, Light Sci. Appl. **9**, 24 (2020).
10. J. F. Algorri, D. C. Zografopoulos, A. Ferraro, B. García-Cámara, R. Beccherelli, and J. M. Sánchez-Pena, Opt. Express **27**, 6320 (2019).
11. K. Koshelev, S. Lepeshov, M. Liu, A. Bogdanov, and Y. Kivshar, Phys. Rev. Lett. **121**, 193903 (2018).
12. P. Jordan, J. von Neumann, and E. P. Wigner, in *The Collected Works of Eugene Paul Wigner* (Springer, 1993), pp. 298–333.
13. C. W. Hsu, B. Zhen, A. D. Stone, J. D. Joannopoulos, and M. Soljačić, Nat. Rev. Mater. **1**, 16048 (2016).
14. Y. Wang, Z. Han, Y. Du, and J. Qin, Nanophotonics **10**, 1295 (2021).
15. S. Xie, C. Xie, S. Xie, J. Zhan, Z. Li, Q. Liu, and G. Tian, Appl. Phys. Express **12**, 125002 (2019).
16. S. Xie, S. Xie, G. Tian, Z. Li, J. Zhan, Q. Liu, and C. Xie, Optik (Stuttgart) **225**, 165761 (2021).
17. J. F. Algorri, F. Dell'Olio, P. Roldán-Varona, L. Rodríguez-Cobo, J. M. López-Higuera, J. M. Sánchez-Pena, and D. C. Zografopoulos, Opt. Express **29**, 10374 (2021).
18. S. Li, C. Zhou, T. Liu, and S. Xiao, Phys. Rev. A **100**, 63803 (2019).
19. S. Han, P. Pitchappa, W. Wang, Y. K. Srivastava, M. V. Rybin, and R. Singh, Adv. Opt. Mater. **9**, 2002001 (2021).
20. X. Chen and W. Fan, Opt. Lett. **44**, 5876 (2019).
21. A. S. Kupriianov, Y. Xu, A. Sayanskiy, V. Dmitriev, Y. S. Kivshar, and V. R. Tuz, Phys. Rev. Appl. **12**, 014024 (2019).
22. P. Yu, A. S. Kupriianov, V. Dmitriev, and V. R. Tuz, J. Appl. Phys. **125**, 143101 (2019).
23. A. Sayanskiy, A. S. Kupriianov, S. Xu, P. Kapitanova, V. Dmitriev, V. V. Khardikov, and V. R. Tuz, Phys. Rev. B **99**, 085306 (2019).
24. A. C. Overvig, S. C. Malek, M. J. Carter, S. Shrestha, and N. Yu, Phys. Rev. B **102**, 035434 (2020).
25. X. Wang, S. Li, and C. Zhou, Opt. Express **28**, 11983 (2020).
26. M. Barrow and J. Phillips, Opt. Lett. **45**, 4348 (2020).
27. A. S. Kupriiannov, K. L. Domina, V. V. Khardikov, A. B. Evlyukhin, and V. R. Tuz, Opt. Lett. **45**, 1527 (2020).
28. M. Wang, B. Li, and W. Wang, J. Opt. **22**, 125102 (2020).
29. J. R. Piper, V. Liu, and S. Fan, Appl. Phys. Lett. **104**, 251110 (2014).
30. L. Zhao, X. Yang, Q. Niu, Z. He, and S. Dong, Opt. Lett. **44**, 3885 (2019).
31. Z. Liu, Y. Xu, Y. Lin, J. Xiang, T. Feng, Q. Cao, J. Li, S. Lan, and J. Liu, Phys. Rev. Lett. **123**, 253901 (2019).
32. C. Tang, B. Yan, Q. Wang, J. Chen, Z. Yan, F. Liu, N. Chen, and C. Sui, Sci. Rep. **7**, 582 (2017).
33. W. Cai and V. Shalaev, *Optical Metamaterials* (Springer, 2010).
34. R. Yahiaoui, K. Hanai, K. Takano, T. Nishida, F. Miyamaru, M. Nakajima, and M. Hangyo, Opt. Lett. **40**, 3197 (2015).
35. J. Algorri, D. Zografopoulos, A. Ferraro, B. García-Cámara, R. Vergaz, R. Beccherelli, and J. Sánchez-Pena, Nanomaterials **9**, 30 (2018).
36. D. Conteduca, I. Barth, G. Pitruzzello, C. P. Reardon, E. R. Martins, and T. F. Krauss, Nat. Commun. **12**, 3293 (2021).
37. S. Chatterjee, E. Shkondin, O. Takayama, A. Fisher, A. Fraiwan, U. A. Gurkan, A. V. Lavrinenko, and G. Strangi, Nano. Adv. **2**, 3452 (2020).
38. N. Li, Z. Xu, Y. Dong, T. Hu, Q. Zhong, Y. H. Fu, S. Zhu, and N. Singh, Nanophotonics **9**, 3071 (2020).